J. Adv. Model. Earth Syst., **Vol. 3**, Art. M04001, 20 pp.

Controls on precipitation and cloudiness in simulations of trade-wind cumulus as observed during RICO

Margreet C. vanZanten[1], Bjorn Stevens[2,3], Louise Nuijens[2,3], A. Pier Siebesma[1,4], A. S. Ackerman[5], F. Burnet[6], A. Cheng[7], F. Couvreux[6], H. Jiang[8], M. Khairoutdinov[9], Y. Kogan[10], D. C. Lewellen[11], D. Mechem[12], K. Nakamura[13], A. Noda[13], B. J. Shipway[14], J. Slawinska[15], S. Wang[16] and A. Wyszogrodzki[17]

[1] Royal Netherlands Meteorological Institute (KNMI) De Bilt, The Netherlands
[2] Max-Planck-Institute für Meteorologie, Hamburg, Germany
[3] Dep't of Atmos.& Ocean Sci., University of California at Los Angeles, Los Angeles, California, USA
[4] Department of Multi-Scale Physics, Delft University, Delft, The Netherlands
[5] Goddard Institute of Space Studies, New York, New York, USA
[6] CNRM/GAME, Meteo-France/CNRS, Toulouse, France
[7] SSAI Inc., Langley Research Center, Washington D.C., USA
[8] CIRA, Colorado State University, Ft. Collins, Colorado USA
[9] School of Marine and Atmospheric Sciences, Stony Brook University, Stony Brook, New York, USA
[10] Cooperative Institute for Mesoscale Meteorological Studies, University of Oklahoma, USA
[11] Department of Mech. and Aero. Engineering, West Virginia University, Morgantown West Virginia, USA
[12] Department of Geography, University of Kansas, Lawrence, Kansas USA
[13] Research Institute for Global Change, Japan Agency for Marine-Earth Science and Technology, Kanagawa, Japan
[14] Met Office, Exeter, UK
[15] Institute of Geophysics, University of Warsaw, Warsaw, Poland
[16] Naval Research Laboratory, Monterey California, USA
[17] NCAR, Research Applications Laboratory, Boulder, Colorado, USA

Manuscript submitted 14 April 2011

Twelve large-eddy simulations, with a wide range of microphysical representations, are compared to each other and to independent measurements. The measurements and the initial and forcing data for the simulations are taken from the undisturbed period of the Rain in Cumulus over the Ocean (RICO) field study. A regional downscaling of meteorological analyses is performed so as to provide forcing data consistent with the measurements. The ensemble average of the simulations plausibly reproduces many features of the observed clouds, including the vertical structure of cloud fraction, profiles of cloud and rain water, and to a lesser degree the population density of rain drops. The simulations do show considerable departures from one another in the representation of the cloud microphysical structure and the ensuant surface precipitation rates, increasingly so for the more simplified microphysical models. There is a robust tendency for simulations that develop rain to produce a shallower, somewhat more stable cloud layer. Relations between cloud cover and precipitation are ambiguous.

DOI: 10.1029/2011MS000056

1. Introduction

The interplay between cloud micro and macrostructure remains poorly understood. Do aerosol or other microphysical perturbations meaningfully regulate the development of precipitation, and how does precipitation influence the macroscopic evolution of clouds? Although answers to these questions vary, it has become clear that the interplay between cloud micro and macrostructure is more subtle than is often appreciated – even for the simplest of cloud regimes (Stevens and Feingold, 2009). In this paper, we combine field measurements with large-eddy simulation (LES) to explore the links between cloud micro and macrostructure and the ability of fine-scale simulations to represent them.

To whom correspondence should be addressed.
Bjorn Stevens, Max-Planck-Institut für Meteorologie, Bundesstrasse 53, Hamburg 20146, Germany
bjorn.stevens@zmaw.de

Scientifically, we develop our questions around a single cloud regime: trade-wind cumuli. Although the clouds in the trade-winds vary in their vertical extent (Riehl, 1954), here we have in mind relatively shallow clouds yet deep enough (2000 m or so) to be susceptible to the development of precipitation. Shallow cumulus clouds such as these have come to be appreciated as a critical piece of the climate puzzle (Bony and Dufresne, 2006; Medeiros et al., 2008) and also serve as perhaps the simplest prototype for precipitating convective clouds.

Methodologically, our framework is that of the GEWEX (Global Energy and Water Experiment) Cloud Systems Studies (GCSS) boundary layer cloud group, through which this intercomparison has been organized. The GCSS framework (Randall et al., 2003) is based on the development of well-defined case studies centered around specific questions, and then explored using as many fine-scale models as can be assembled. The goal of such a procedure is not to identically reproduce the data from which the case-studies are often drawn, but rather to identify the extent to which robust behavior emerges across a suite of simulations produced using different numerical methods and physical parameterizations. In the present context such behavior might include the character of precipitation as a function of the cloud evolution, or the response of the cloud field to the development of precipitation. To the extent one can identify such behavior, one is encouraged in the development of rules or constraints that can be exploited when building parameterizations. This idea, of using LES to improve parameterizations by filling in process-level details that are missing in observations of cloudy boundary layers, is at the heart of the GCSS approach.

In practice, the act of defining the cases has taught us as much about the LES technique, and its limitations, as it has about the interplay of processes that determine the macroscopic characteristics of observed cloudy boundary layers. For instance, through the work of GCSS it has become clear that, to the extent the simulated flow depends on the character of mixing in regions where the length-scale of the turbulence ceases to be as large as compared to that resolvable by the simulations, significant differences can emerge as a function of ones choice of numerical methods, or sub-grid closure (Stevens et al., 2005). Isolating which source of error dominates is in practice quite difficult (Ghosal, 1996; Stevens et al., 2000). Additionally, recent work concentrating on stratocumulus has shown that quantitative estimates of precipitation can vary greatly among models, depending in uncertain ways on the representation of cloud microphysical processes within LES. And in certain situations this can even impact the overall statistics of the simulations (Ackerman et al., 2009). As a result, the case-studies developed by GCSS have developed into important benchmarks for the broader scientific community.

Despite methodological uncertainties, by carefully posing problems it often has proved possible to use LES in the manner initially envisioned, that is, to constrain or improve parameterizations of cloudy boundary-layers. For instance, studies of the stratocumulus as measured during DYCOMS-II have helped place upper bounds on entrainment (Stevens et al., 2005). Because such bounds are inconsistent with the hypothesis that entrainment can be significantly enhanced by buoyancy-reversal processes alone (cf., Deardorff, 1980), the community has been forced to re-evaluate (and increasingly reject) the idea that such processes may play a role in determining basic features of the stratocumulus cloud climatology. Likewise, LES has shown that the entrainment rate in stratocumulus depends on the precipitation flux, even that associated with the weak sedimentation of cloud droplets. Less cloud-top entrainment is associated with enhanced cloud-top droplet sedimentation (Ackerman et al., 2004; Bretherton et al., 2006; Ackerman et al., 2009). This basic finding has made an important contribution to our evolving understanding of how stratocumulus layers respond to perturbations in their precipitation efficiency. Likewise, our understanding of lateral entrainment through the sides of shallow cumulus (Siebesma and Cuijpers, 1995) has been consolidated through a series of case studies developed by the GCSS (Stevens et al., 2001; Brown et al., 2002; Siebesma et al., 2003).

In the present study we use data abstracted from the Rain in Cumulus over the Ocean (RICO) Field Campaign (Rauber et al., 2007) to define a reference case for LES of precipitating cumulus-topped boundary layers[1], and evaluate the representation of the boundary layer from an ensemble of large-eddy simulations. Our goals are threefold: (i) methodologically, we wish to understand if LES can plausibly represent the microphysical evolution of trade-wind cumulus convection, and how sensitive the representation of precipitation is to ones choice of microphysical model; (ii) physically, we wish to explore whether precipitation robustly retards the growth of the cumulus layer, as hypothesized by Stevens (2007), and reduces cloud amount as hypothesized by Albrecht (1989); and (iii) practically, we wish to contribute to the growing suite of benchmark cases that have been developed and explored through the efforts of the GCSS boundary layer working group.

The remainder of this study is organized as follows. In §2, we describe the construction and characteristics of the reference case and the participating LES codes. §3 reviews the basic behavior of the simulations. §4 explores the simulations in light of observations from RICO, with a focus on the development of precipitation and the cloud microphysical structure. §5 addresses methodological question raised above, as to how sensitive precipitation formation in these clouds is to the details of their microphysical representation. The physical questions relating to the effects of precipitation on the simulation are taken up in §6. Conclusions are presented in §7.

[1] Here we think of the cumulus filling the upper portion of the boundary layer, as we identify the boundary layer as the layer in which surface bounded vertical transport by turbulent eddies is a dominant process.

Journal of Advances in Modeling Earth Systems james_000056.3d 24/5/11 09:57:45
The Charlesworth Group, Wakefield +44(0)1924 369598 - Rev 7.51n/W (Jan 20 2003)

2. Case Definition

2.1. Data sources

The simulations are based on data collected during the Rain in Cumulus over the Ocean (RICO) field study. RICO was a comprehensive field study of shallow cumulus convection which was located in the winter trade-winds of the northwestern Atlantic ocean, just upwind of the Islands of Antigua and Barbuda. An overview of the experiment is provided by Rauber et al. (2007). One focus of RICO was on the statistical character of the cloudy boundary layer, particularly on the characterization of precipitation in shallow cumulus. This focus distinguishes RICO from earlier studies such as the Barbados Oceanographic and Meteorological Experiment (BOMEX Holland, 1972) and the Atlantic Trade-wind Experiment (ATEX Augstein et al, 1973), which measured little in the way of clouds and precipitation.

The RICO study area from which our data is drawn corresponds to the NE quadrant of a circular area some 300 km in diameter, centered around the Island of Barbuda. This study area almost always had a precipitating cloud within it, and while precipitation from individual clouds could be intense (individual echoes from 3000–4000 m deep clouds could reach above 50 dBZ) precipitation averaged over the area as a whole was modest (Nuijens et al., 2009).

The data naturally identify an undisturbed period between December 16 2004 and January 8 2005. Using a reflectivity rain-rate relationship developed for shallow convection during TRMM (Schumacher and R. Houze Jr., 2003; Short and Nakamura, 2000), we estimate that precipitation fluctuated about a mean value of about 21 W m^{-2}, which is just less than 1 mm d^{-1}. This is illustrated by Fig. 1 which presents the area-averaged rain rates derived from nearly horizontal surveillance scans (performed every 20 minutes). Although not shown, the fraction of the observed area with identifiable radar echoes averages about 3 % and varies in proportion to the overall area rain rate (Nuijens et al., 2009).

In Fig. 1, and in subsequent figures, we generally present precipitation in energetic units, as this reflects our primary interest in the energetics of the layers being studied. Depending on ones purpose or background however other representations of precipitation can be more common. In Table 1 we summarize how sensitive the estimated rain-rates are to the chosen R-Z (rainrate-reflectivity) relationship and present numbers in both mass and energy units for future reference.

Because the RICO measurement strategy was developed around the idea of constraining the temporally and spatially averaged statistics of the lower troposphere over many days, the data were not well suited to the definition of a case study drawn from a particular 6–10 hr research flight. Unlike in past studies, RICO did not employ a sounding array so as to constrain spatial gradients, and hence large-scale forcing, in the atmospheric state. Hence, important aspects of the forcing, such as moisture advection and vertical velocity, were not directly measured.

To estimate the mean forcing during the undisturbed RICO period, we downscaled European Centre for Medium Range Weather Forecasts to LES sized domains using the Regional Atmospheric Climate Model (RACMO Meijgaard et al., 2008). RACMO uses the same physical parameterizations as the ECMWF integrated forecast system (IFS), but on a finer (20 km) grid, and thus is well suited for these purposes. RACMO hind-cast simulations were performed for the entire two month (December 2004 through January 2005) period over a 1800 × 1800 km^2 domain containing the RICO research area. New simulations were initialized every twenty-four hours using the 1200 UTC ECMWF analysis. Output was generated every 10 minutes on a 5° × 5° grid centered around the RICO research area. A comparison between RACMO and the two month surface precipitation time series from the S-Pol radar data suggested that RACMO had some skill in representing the general regime. RACMO averaged roughly 60 W m^{-2} of surface precipitation, compared to the 35 W m^{-2} inferred from the radar, and it did show enhanced precipitation in association with the mid December 2004 and early January 2005 rainy periods, although overall it had much less contrast between wet and dry periods. All in all this analysis, and the lack of better alternatives, motivated the use of RACMO to help

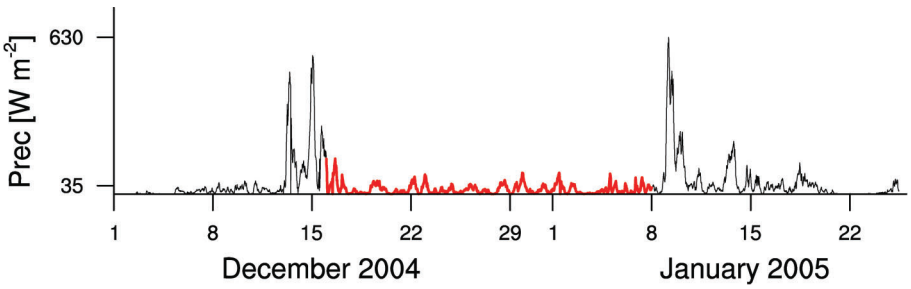

Figure 1. Area averaged precipitation for each S-pol radar (0.5°) surveillance scan plotted for the months of December 2004 and January 2005. The thick red line indicates what we refer to as the undisturbed period over which we composite (see text). Ordinate values denote the maximum and average precipitation for the entire period.

Journal of Advances in Modeling Earth Systems james_000056.3d 24/5/11 09:57:45
The Charlesworth Group, Wakefield +44(0)1924 369598 - Rev 7.51n/W (Jan 20 2003)

Table 1. Rain rate conversion factors, where the conversion to dBz is based on the TRMM shallow convection algorithm, whereby $Z=148R^{1.55}$ with R measured in mm d^{-1}, and on the (Snodgrass et al., 2009) reflectivity rain-rate relationship that has been developed based on *in situ* rain-shaft sampling during RICO.

mm d^{-1}	W m^{-2}	dBZ (TRMM)	dBZ (RICO)
1.0	28.5	0.3	−1.5
3.5	100.0	8.7	6.8
2.7	77.0	7.0	5.1
82.3	2346.2	30.0	27.6

constrain estimates of quantities, such as the large-scale forcing, that were poorly measured during RICO.

However, even with this approach it was difficult to match the day to day variability seen during RICO with that simulated using RACMO. This suggests that the mesoscale forcing provided to RACMO by the ECMWF analysis did not significantly constrain the behavior on any particular day. For these reasons, attempts to define a reference case based on measurements on a single day were abandoned in favor of a more idealized case based on the composite structure of the atmosphere over this undisturbed period. Qualitatively, the composite lies within the span of the samples and thus constitutes a plausible day during the RICO study period.

2.2. Initial and forcing data

2.2.1. Initial state

The initial profiles of potential temperature θ, specific humidity q_v and the horizontal winds u and v are constructed as piece-wise linear fits of the averaged profiles from those radiosondes launched 2–6 times daily from Spanish Point (Barbuda), during the undisturbed period. Figure 2 and Table 2 present the mean radiosonde profiles together with initial profiles. The geostrophic wind did not vary with time and is used also as the initial wind profile. The initial state is chosen to have as simple a vertical structure as possible given the uncertainty range of the measurements. The main motivation for doing so was twofold: (i) for such profiles it is easier to construct a forcing whose different components sum to zero away from regions where turbulent fluxes are expected to be important; (ii) simple profiles identify fewer parameters and thus facilitate sensitivity studies.

Compared to the BOMEX and ATEX case studies, which sampled a similar cloud regime (Siebesma et al., 2003; Stevens et al., 2001) the mean tropospheric temperatures are somewhat warmer, 317 K at 4000 m for the present case as compared to 316 K during BOMEX and 315 K during ATEX. For BOMEX and ATEX, SSTs were taken as 298 K and 300.4 K respectively, as compared to 299.8 K for the present case. Hence the lower tropospheric stability was somewhat less during BOMEX and greater during ATEX. The free troposphere above 3260 m was considerably moister during ATEX (4.5 g kg^{-1} as compared to less than 2.4 g kg^{-1}), and similarly dry (implicitly 2.7 g kg^{-1} at 3260 km decreasing to 1.8 g kg^{-1} at 4000 m) during BOMEX.

2.2.2. Forcing

Vertical profiles of the subsidence rate and temperature and moisture tendencies due to horizontal advection have been constructed from the RACMO data and are specified in table 2. In general these forcings are more favorable for convection than what was applied for the BOMEX and ATEX cases, with stronger large-scale cooling and less drying in the present case. The large-scale cooling incorporates both the radiative and advective cooling in the Eulerian frame. Note that for the simulations most groups only considered the effect of subsidence on the thermodynamic quantities. The WVU simulations applied subsidence tendencies to all prognostic variables, although there was no indication that this made an important difference to the outcomes.

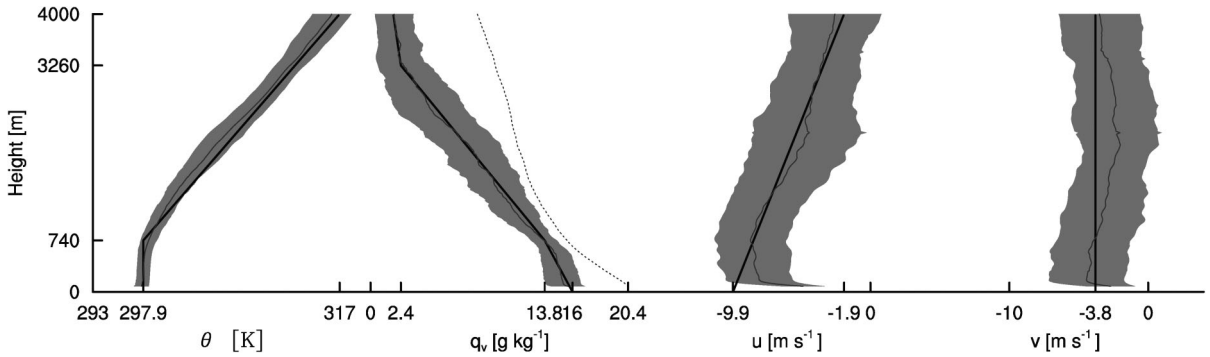

Figure 2. Mean profiles of potential temperature θ, specific humidity q_v and the zonal and meridional wind components u and v of all radiosondes released from Spanish Point in the period from 16 Dec 2004 through 8 Jan 2005, here shown by thin black line. The shaded area denotes the interquartile (first to third) range. The dotted black line in the second panel indicates the mean profile of saturation specific humidity during this period. The specified initial profiles for the composite case are shown by the thick black line.

Journal of Advances in Modeling Earth Systems james_000056.3d 24/5/11 09:57:46
The Charlesworth Group, Wakefield +44(0)1924 369598 - Rev 7.51n/W (Jan 20 2003)

Table 2. Fixed points for piecewise linear profiles of θ, q_v, u, v, the subsidence rate W and the large scale forcing of heat and moisture. The large scale thermal (potential temperature) forcing is a combination of both the net radiative forcing and the horizontal advection of temperature.

Height	θ	q_v	u	v	W	$\partial_t\theta\|_{LS}$	$\partial_t q_v\|_{LS}$
[m]	[K]	[g kg^{-1}]	[m s^{-1}]	[m s^{-1}]	[cm s^{-1}]	[K day^{-1}]	[g kg^{-1} day^{-1}]
0	297.9	16.0	−9.9	−3.8	0.0	−2.5	−1.0
740	297.9	13.8	–	–	–	–	–
2260	–	–	–	–	−0.5	–	–
2980	–	–	–	–	–	–	0.3456
3260	–	2.4	–	–	–	–	–
4000	317.0	1.8	−1.9	−3.8	−0.5	−2.5	0.3456

In line with previous trade-wind cumulus intercomparison studies, a net radiative forcing is prescribed instead of being computed by an interactive radiation scheme. The motivation for doing so partly reflects our focus on the fluid-dynamical-microphysical interactions, and past experience that suggests that interactive radiation is not necessary to capture the leading order dynamics of the cumulus-topped boundary layer in the absence of overlying stratiform layers. The applied net radiative tendency has been obtained by using an offline ECMWF radiation scheme initialized with the above described profiles of temperature and humidity. By averaging the results over twenty-four hours, we obtained a profile that prescribes a cooling rate of 2 K day^{-1} close to the surface, decreasing to about 1 K day^{-1} in the free atmosphere.

The surface momentum fluxes and thermodynamic fluxes are parametrized using bulk aerodynamic formulae, such that

$$\overline{w'\theta'} = -C_h \|U\| \left(\theta - \theta|_{z=0}\right), \tag{1}$$

$$\overline{w'q_{t'}} = -C_q \|U\| \left(q_t - q_{sat}|_{z=0}\right), \tag{2}$$

$$\overline{u'w'} = -C_m \|U\| u, \tag{3}$$

$$\overline{v'w'} = -C_m \|U\| v, \tag{4}$$

where we specified C_m=0.001229, C_h=0.001094 and C_q=0.001133. The sea-surface temperature, $T_{z=0}$ was also fixed at 299.8 K. The wind speed $\|U\|$ was taken from the model near surface winds. Because the vertical grid was chosen to be 40 m, this implied that most models located their near surface winds at 20 m. For models having near surface winds valid at a different heights transfer coefficients were specified to be scaled following (Stevens et al., 2001). Surface fluxes constructed in this manner were found to well approximate those that were actually measured during the latter part of the RICO field study, when a research vessel was in the area (Nuijens et al., 2009).

Combining the specified large-scale forcing with the surface fluxes as parametrized, and assuming an additional term for precipitation of 21 W m^{-2} (the average precipitation flux, using the TRMM *Z-R* relationship, during the undisturbed composite period obtained from the S-Pol radar observations) leads to vertically integrated total budgets of heat and moisture which are approximately closed. Additionally, the net large scale forcing in the upper part of the LES domain, away from the turbulent circulations, was set to zero by construction.

2.2.3. Microphysics

To explore the role of microphysical effects, we perform simulations that allow for the active evolution of the cloud microphysical structure, through microphysical (droplet kinetic) processes. The starting point for such simulations is a specification of the droplet population density, or the cloud-condensation nuclei (CCN) population density, depending on how a particular model is formulated.

For models which employ a fixed cloud-droplet population density the concentration was set at 70 cm^{-3}. This value is based on a average of best estimates (ranging from 50 to 100 cm^{-3}) of the active cloud-droplet population density of four (out of six) flights during the composite period as measured by the Fast Forward Scattering Spectrometer Probe (FFSSP) instrument (Brenguier et al., 1998). The active cloud-droplet population density is taken by sub-sampling nearly adiabatic updrafts within the cloud, and it is thought to be the best single number to represent the droplet amount playing a role in rain formation (Pawlowska and Brenguier, 2000, 2003). The active cloud droplet population density during the undisturbed period of RICO is roughly 20 to 30 cm^{-3} higher than a straightforward cloud droplet population density averaged over all cloudy points. The sensitivity of precipitation development to droplet population densities is explored with one of the LES codes in Stevens and Seifert (2008).

For models that predict the cloud-droplet activation spectrum, the CCN spectrum is assumed fixed with a population density of 100 cm^{-3} at 1% supersaturation; this number is loosely based on data from the RICO campaign (James Hudson, personal communication, 2007). The shape of the distribution, if required by a model, is based on *in situ* (PCASP) data from research flight 12 (RF12). These data were approximated by a bimodal log-normal distribution of ammonium-bisulfate whose geometric mean radii of 0.03

and 0.14 μm, geometric standard deviations of 1.28 and 1.75 μm and CCN population densities of 90 and 15 cm^{-3} for the first and second mode respectively, lead to an integrated CCN population density of roughly 100 cm^{-3} at 1% supersaturation.

2.3. Participating groups

A total of twelve research groups successfully simulated the case using LES. In addition one group simulated the case with a 2D model, albeit employing higher-order closures. Information about the various models can be found in Table 3. SAM, SAMEX and 2DSAM have an (almost) identical dynamical core with 2DSAM being the two dimensional version of SAM, and SAMEX being SAM with an explicit microphysical scheme.

The microphysical parameterizations used by the various groups can be divided into three groups based on how the size distribution of cloud and rain drops is discretized. Most groups use a bulk scheme wherein one (total mass of rain) or two (mass and number) moments of the drop distribution are prognosed. For the groups using two-moment bulk schemes, only two moments of the rain-drop distribution are modeled - cloud water mass is inferred from an equilibrium assumption. A few groups use non-parametric approaches wherein the full distribution is modeled by discretizing the size distribution. These latter schemes are more fundamental than bulk approaches, but because they endeavor to resolve the entire droplet distribution, they are computationally more expensive. Indeed the computational demands of fully resolving the evolution of the droplet spectrum are often only partially met, which means that different implementations of such approaches can differ substantially from one another as a result of their numerical implementation. To distinguish them from the bulk models they are referred to as bin models as the droplet distribution is represented discretely by a number of bins, or size categories. Microphysical schemes may additionally differ in how, or whether they include processes. The MESO-NH model and the Met Office LEM include ventilation effects in their representation of evaporation, DALES and the WVU models are the only ones with a two moment scheme that includes sedimentation of cloud droplets.

Several models (*i.e.*, DHARMA, UCLA, WVU, COAMPS, MetO, SAM, NHM, RAMS) participated in the drizzling stratocumulus intercomparison case (Ackerman et al., 2009) and of those models further information on their microphysical schemes can be found in Appendix B of Ackerman et al., (2009). In the case of the MetO model a different fall-speed relationship has been used in the present study; see Abel and Shipway (2007) for more details. MESO-NH and WVU include a sub-grid-scale condensation parameterization, but the results are not very sensitive to this innovation.

2.4. Experimental protocol

2.4.1. Model setup

Participants were asked to perform simulations with and without droplet kinetics. Simulations with droplet kinetics

Table 3. Model list and lead scientist name, configuration of the model and the amount of surface precipitation generated over the last four hours of the precipitating simulation. Four flavors of sub-grid scale (SGS) models are used: HoT refers to the higher (3rd) order closure used by the 2D model, 2DSAM; DL refers to the prognostic TKE approach of Deardorff (1980) and Lewellen (1977); SL refers to the Smagorinsky-Lilly approach; and DS revers to the dynamical version of the Smagorinsky model. Advection of momentum and scalars are some flavor of monotone or positive definite (denoted by M) or centered (denoted by C). The simulations are grouped in three categories as a function of the complexity of their microphysical representation, with the one moment models first, followed by the two-moment models, followed by the bin models. The microphysical schemes are identified in the case of the most commonly used schemes, these being: SB following Seifert and Beheng (2001) and Seifert and Beheng (2006); KK following Khairoutdinov and Kogan (2000), with KK$_s$ as a simplified version of the KK scheme. For the three moment schemes the scheme is identified by the number of bins used to represent the drop spectrum.

LES name	scientist	SGS	mom.	scal.	microph.	P_{srf}
			adv.	adv.	scheme	[W m^{-2}]
1 Moment Schemes						
2DSAM	A. Cheng	HoT	M	C	KK$_s$	31.2
EULAG	J. Slawinska	SL	M	M		13.8
MESO-NH	F. Couvreux	DL	C	C		25.9
NHM	A. Noda	DL	C	C		12.7
SAM	M. Khairoutdinov	DL	M	C	KK$_s$	11.1
2 Moment Schemes						
COAMPS	S. Wang	DL	C	M	KK	5.5
DALES	M.C. van Zanten	DL	C	C	SB	2.5
MetO	B. Shipway	SL	C	C		26.7
UCLA	B. Stevens	SL	C	M	SB	2.3
WVU	D.C. Lewellen	DL	C	M	KK	0.0
Bin Schemes						
DHARMA	A.S. Ackerman	DS	M	M	25	5.9
RAMS	H. Jiang	DL	C	M	66	0.1
SAMEX	D. Mechem	DL	M	C	34	7.5

Journal of Advances in Modeling Earth Systems james_000056.3d 24/5/11 09:57:47
The Charlesworth Group, Wakefield +44(0)1924 369598 - Rev 7.51n/W (Jan 20 2003)

are often referred to as precipitating simulations although precipitation does not necessarily develop. In the absence of droplet kinetics, rain will not develop, and liquid water can be derived diagnostically. In this limit, for those models that also neglect the sedimentation of cloud droplets, liquid water follows the fluid motion to within the accuracy of the numerical solvers. A duration time of 24 hr was chosen for the simulations in order to allow plenty of time for the development of a mean state that could support precipitating clouds in the case when droplet kinetics were turned on. The horizontal domain was specified to be 12.8 by 12.8 km, solved with 128 grid points in each horizontal direction and 100 in the vertical (equally spaced in 40 m increments). Sensitivity studies at a variety of resolutions and domain sizes (including much finer grids spanning a larger area) were performed by a number of groups (*e.g.*, Stevens and Seifert 2008; Nuijens, 2010; Matheou et al., 2010).

2.4.2. Analysis methods

Each group was asked to standardize their output following the variable list provided in tables 4–6 in the appendix. The required output consists of hourly averaged profile data, including fluxes and conditionally sampled fields, as well as more frequent output of scalar quantities. Subsequent analysis is based on this standardized output.

From this output two 'master' ensembles, one for the precipitating case and another for the non-precipitating case, have been constructed from all of the three dimensional models that submitted results consistent with the case specification.

Our analysis is centered over the last four hours of the simulation, unless otherwise noted. For the relatively small domain we simulate, relatively few precipitating clouds, or cloud clusters are evident in the domain at any given time. This means that the domain-averaged precipitation signal fluctuates significantly in time and incoherently among models. Such fluctuations are still pronounced for domains whose area is an order of magnitude larger. Hence the averaging period was chosen to ameliorate the effects of these fluctuations as the life-time of any particular event is on the order of tens of minutes to an hour.

For some of the analysis, conditional sampling over cumulus clouds is performed, following the cloud ($q_c >$ 0.01 g kg^{-1}) and cloud-core ($q_c >$ 0.01 g kg^{-1} and positively buoyant) criteria used in previous studies (Siebesma et al., 2003). In addition two further sampling criteria were introduced for purposes of our analysis. One criteria identifies rain-water grid boxes as ones in which rain water q_r is present above a threshold of 0.001 g kg^{-1}. The other criteria identified precipitating grid boxes as ones in which the precipitation flux is higher than 3.65×10^{-5} kg kg^{-1} m s^{-1}. The first is used to calculate a mean rain drop population over rainy grid boxes only. The second is applied in the calculation of conditionally sampled precipitation fluxes. The threshold for a grid-box to be defined as rainy is chosen to equal the cutoff precipitation flux of the S-Pol radar data, given the assumed S-Pol rain-reflectivity relationship.

3. Simulated evolution and structure

3.1. General structure

The simulations paint a consistent picture of the general cloud structure, one that conforms with our understanding of the structure of the trade-wind region as has been developed on the basis of many past studies (*e.g.*, Malkus, 1956; Nitta and Esbensen, 1974; Sommeria, 1976; Stevens et al., 2001; Siebesma et al., 2003). This is illustrated by Figs. 3 and 4, where we focus on the interquartile variability (the dark gray areas showing the spread of the central fifty percent of the distribution). Because the simulation domain is relatively small, the temporal variability is sensitive to the evolution of the one or two larger cloud clusters that develop within it. For many variables, particularly the cloud and precipitation related statistics in the right half of Fig. 3, this temporal variability dominates the full spread among simulations.

The first couple of hours of simulation time are dominated by the spin-up of the turbulence and the initial development of the cloud layer. A longer adjustment timescale is also evident in the thermodynamic state of the subcloud layer: latent heat fluxes initially decrease, reaching a minimum after about eight hours, and cloud base height evolves more markedly over the first twelve hours than it does thereafter. In the second half of the simulation period the temporal evolution is modest but secular. The layer deepens continuously, latent heat fluxes increase as more dry air is brought to the surface, the mass flux and cloud cover remain relatively constant, while the liquid water path and the rain water path increase in association with the deepening cloud layer (Fig. 3). Values of cloud cover, surface fluxes, and the general depth of the convective layer are consistent with observations during RICO, (*e.g.*, Nuijens et al., 2009) as well as past observations of trade-wind clouds.

The vertical structure of the clouds is also consistent with the general picture of such cloud layers as has been developed over the years. Cloud fraction peaks near cloud base, where low-level winds maximize and moisture gradients are relatively large (compare Fig. 4 with Stevens et al., 2001). More significant differences among the simulations are evident near cloud top (around 2300 m), where simulations show, to differing degrees, the emergence of local maxima in liquid water and cloud fraction (lower panels of Fig. 4). These differences are also associated with the development of a sharp increase in static stability, as measured by the increase in $\mathrm{d}\theta_l/\mathrm{d}z$ as compared to its

Journal of Advances in Modeling Earth Systems james_000056.3d 24/5/11 09:57:47
The Charlesworth Group, Wakefield +44(0)1924 369598 - Rev 7.51n/W (Jan 20 2003)

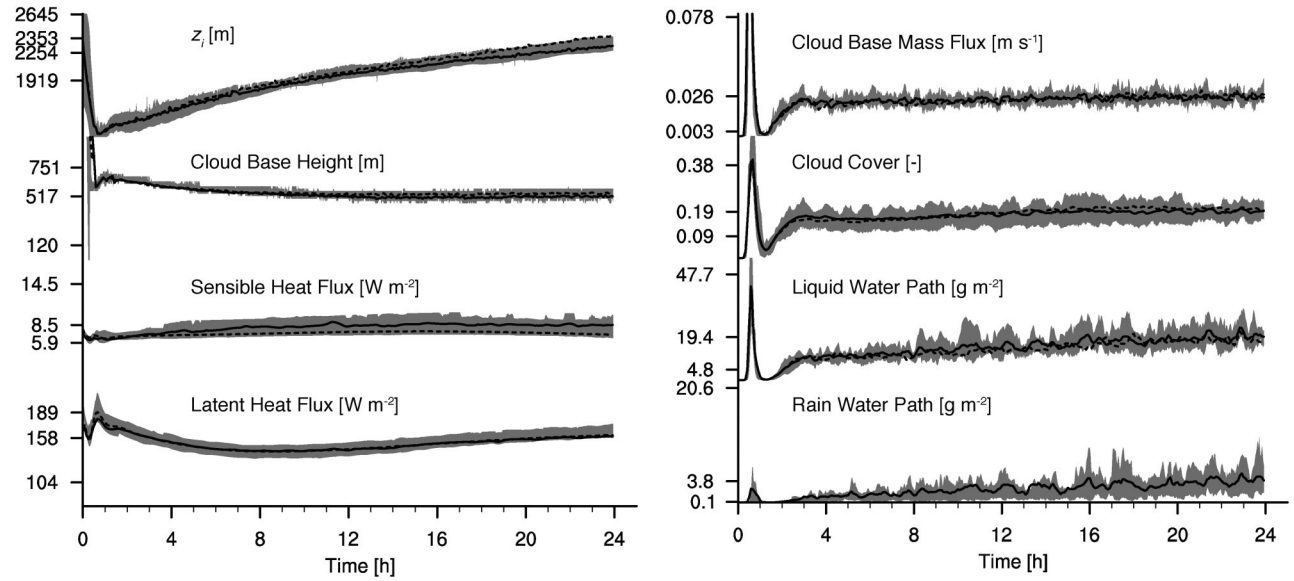

Figure 3. Time series of various simulation diagnostics (see Appendix for a full listing and nomenclature): inversion height, z_i; lowest cloud base, z_{cb}; surface sensible, $\rho_0 c_p \overline{w'\theta'}$, and latent, $\rho_0 L_v \overline{w' q_{t'}}$, heat flux; cloud core mass-flux at the height of the largest cloud fraction; fraction of cloudy columns *cc*; liquid water path, LWP; and rain water path, RWP. Both the mean of the simulations in which precipitation is allowed to develop (solid line) and prohibited (dashed line) are shown. Ensemble (inter-quartile) spread is given by the shading. Ensemble spread is shown only for the precipitating simulations, although results for the non-precipitating ensemble are similar. The ordinate values represent statistics over the last four hours of the simulation, respectively the minimum and maximum value (for the full ensemble) and the four hour mean, except for z_i where the four hour mean of the no precipitation ensemble is also included.

initial value at that level. Note that this zone of enhanced stability (the trade-inversion) develops spontaneously among the simulations. In contrast to past intercomparison cases of trade-wind convection, such a feature was not specified as part of the initial conditions. The somewhat larger differences that develop among the simulations in this region are not surprising, as the turbulent eddies are not well resolved by our grid-mesh in these zones of more marked stability (cf., Stevens et al., 2001).

Experiments in which the RICO case was rerun using a single model (in this case the UCLA-LES Matheou et al., 2010; Nuijens, 2010), but with different numerical schemes for advection, time-stepping, or even the mean wind used in the Galilean transform, produced commensurate (or even larger) differences as those shown across the models here. In these tests the representation of scalar advection and the still relatively coarse computational mesh emerge as key issues.

Important for the parameterization of clouds and precipitation is the vertical structure of the mass flux, updrafts, and the entrainment/detrainment length-scales (Siebesma and Cuijpers, 1995). In their summary of existing studies, Siebesma et al. (2003) argued that a mass flux profile that maximizes near cloud base and decreases through the cloud layer, is a generic feature of the trade-wind cloud layer. Such a structure is less marked in our simulations (e.g., Fig 5), where the mass flux is more constant with height through the bulk of the cloud layer. In retrospect, the lack of a marked decrease in the mass flux through the cloud layer is also evident in the simulations of shallow cumulus convection observed during ATEX (Stevens et al., 2001). This raises the possibility that the shape of the mass flux profile is more sensitive to environmental factors than has previously been acknowledged, and for which a new hypothesis has been recently put forward by de Rooy and Siebesma (2008). Conditionally sampled vertical velocities within the cloud layer of the present simulations are somewhat larger and the entrainment/detrainment rates are somewhat smaller than for either BOMEX or ATEX, both of which likely reflect the nearly two-fold deeper cloud layers simulated in the present case.

3.2. Development of precipitation

Although the general evolution and structure of the cloud field is quite similar among models, the same cannot be said about the development of precipitation. Among the inter-quartile of the simulations one can find a many fold difference in the rain-water path (bottom right panel of Fig. 3) as well as the surface precipitation (Table 3). The variability in rain rates is also shown in Fig. 6. All but two of the simulations develop sufficient precipitation to reach the surface by the final four hours of the simulated cloud evolution, but how soon precipitation develops and the amount that develops varies greatly from one simulation to another.

Journal of Advances in Modeling Earth Systems james_000056.3d 24/5/11 09:57:47
The Charlesworth Group, Wakefield +44(0)1924 369598 - Rev 7.51n/W (Jan 20 2003)

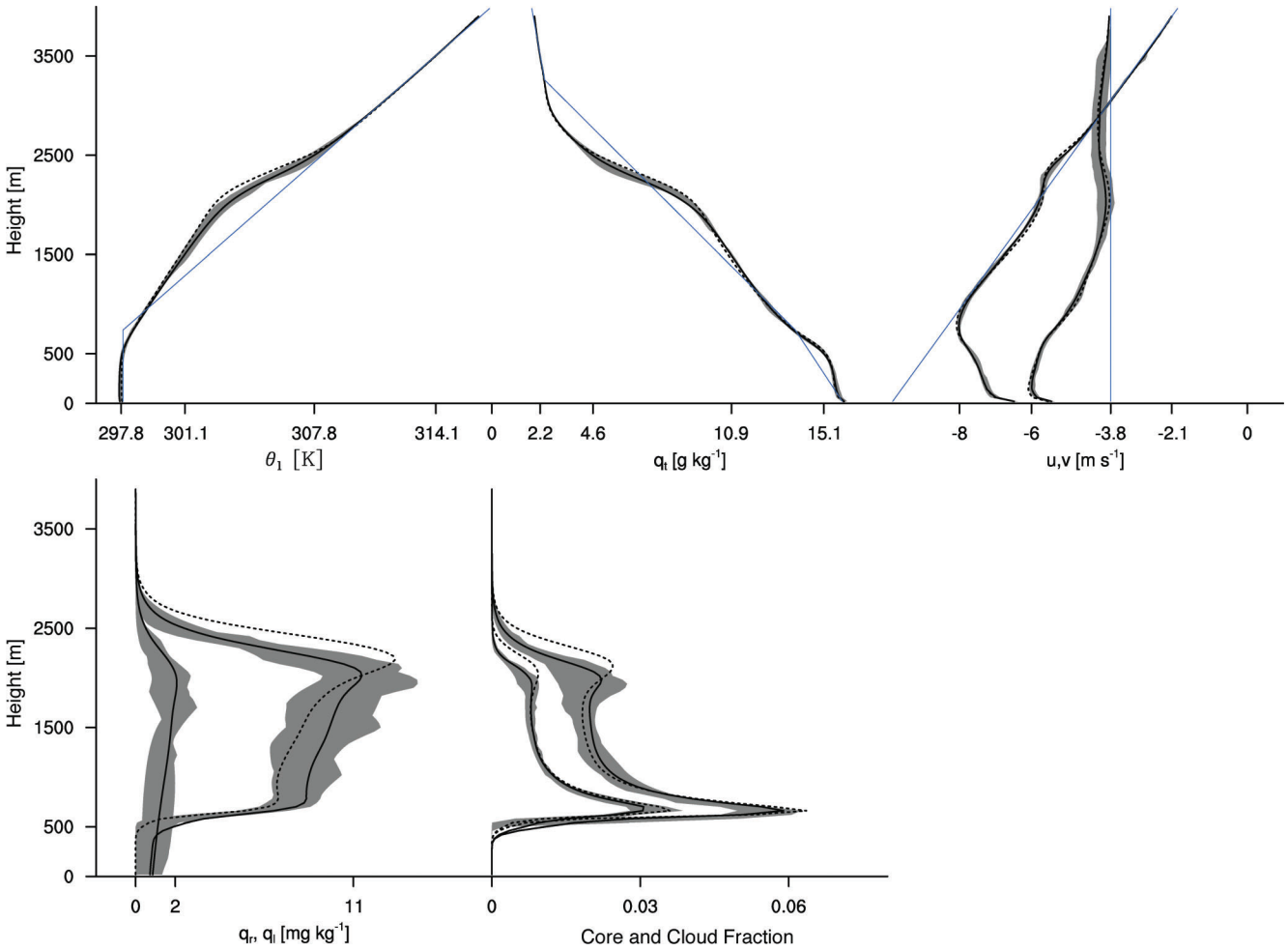

Figure 4. Mean thermodynamic state of the last four hours of the precipitating (solid line) and no precipitation (dashed line) ensemble. Profiles shown are of the liquid water potential temperature θ_l, total water specific humidity q_t, horizontal winds u and v, condensed water q_l and rain water q_r and cloud and cloud core fraction. The shading convention follows that of the previous figure, with the thin dashed line showing the mean profiles from the non-precipitating simulations. The thin blue lines denote the initial conditions.

As compared to other quantities we have explored, the vertical structure and character of the precipitation field among the simulations differ more markedly. Even so, some points of agreement among the simulations emerge. An interesting one is the tendency of the precipitation flux to maximize at cloud top (Fig. 6). If precipitation principally fell through a well developed cloud, one would expect, as is the case for stratocumulus, the precipitation rate to maximize near cloud base. As it is, the simulations show, albeit less markedly among the one-moment schemes, that the evaporation of precipitation is concentrated in the cloud-layer itself. This may result from the fact that in many cases the precipitation forms near the end of the cloud lifecycle (Stevens and Seifert, 2008), or because of vertical shear, so that rain that develops near cloud top falls outside of the clouds tilted by the vertical shear of the horizontal winds.

By dividing the precipitation rate by the mass of rain water one can derive a bulk fall speed for hydrometeors, profiles of which are shown in the upper panel of Fig. 6. The simulations differ both in terms of the effective fall speed of the hydrometeors they produce and the variation of this fall speed with height. There does not appear to be a strong relationship between how much rain is produced by a model, and the size of the raindrops as measured by the bulk fall speed of the rain. The bin and two moment schemes do show a consistent evolution toward larger bulk fall velocities as the surface is approached, a feature that the one moment schemes appear incapable of representing.

Based on this analysis there is little evidence that the actual amount of precipitation is more robustly determined by one class of scheme than the other. Precipitation rates vary as much among the bin schemes as they do among the one moment schemes. However, if one is interested in the structure of the precipitation field, including for instance the distribution of evaporation in the cloud versus subcloud layer, there is some evidence that such features are systematically distorted by the one-moment schemes.

Journal of Advances in Modeling Earth Systems james_000056.3d 24/5/11 09:57:48
The Charlesworth Group, Wakefield +44(0)1924 369598 - Rev 7.51n/W (Jan 20 2003)

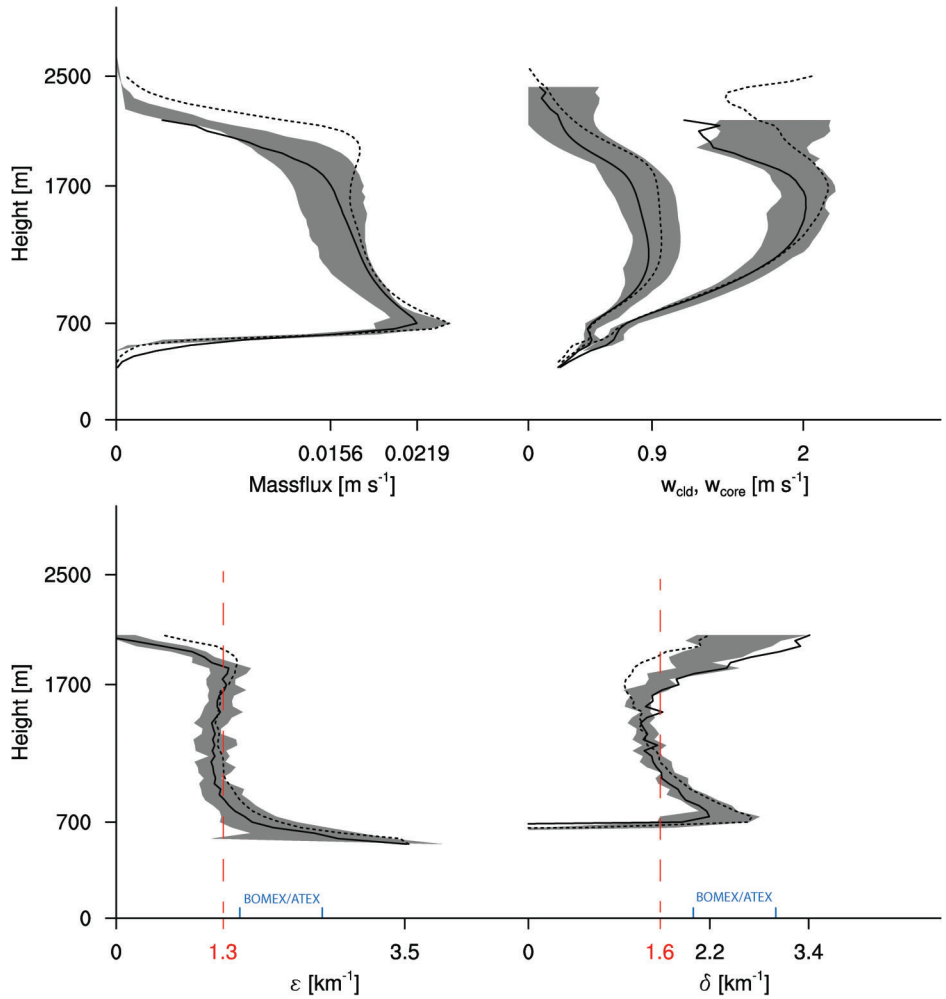

Figure 5. Profiles of core mass-flux, cloudy and core vertical velocity, fractional entrainment rate ε and fractional detainment rate δ averaged over the last four hours of the simulations. Entrainment and detrainment rates are diagnosed using Eq. 16 of (Stevens et al., 2001) for q_t . Lines and shadings follow the conventions of Fig. 3. The mean value in the cloud layer of ε and δ is denoted in red, and the range of values as encountered in the BOMEX and ATEX case is also indicated in blue.

4. Observational Constraints

As compared to previous case studies of clouds in the trade-winds, RICO has the advantage of a great wealth of *in situ* and remote sensing data — particularly of the clouds themselves. In this section we attempt to exploit this wealth of data, although several factors conspire to make this more challenging to do so, at least in a decisive way. Underlying all of the challenges is the sampling issue. Our case-study is based on the composite forcing, which means that the behavior of the simulated clouds cannot *a priori* match any particular day, but should fall within the range of observed cases on similar days. However, similar days are relatively infrequent, because the composite period falls in between the intensive field operations, when aircraft data are more sparse. The *in situ* measurements that are available are biased by a flight strategy that sought to maximize penetrations of active cumuli growing through the flight level. For instance, a comparison between LES and airplane observations of the RICO campaign by Heus et al. (2009) showed a discrepancy in cloud cover, cloud (size-) distribution and in in-cloud velocity; however the differences between models and observations were demonstrated to mostly vanish if the airplane's bias towards larger clouds was taken into account. Although these issues complicate efforts to make decisive statements, the type of comparisons we are able to make still represent a great step forward in studies of cumulus convection.

A basic question is whether the simulated cloud cover is consistent with what was observed. The median cloud cover among the simulations, averaged over the last four hours, is 0.19, which compares favorably with the value of 0.17 obtained through an analysis of lidar data (Nuijens et al., 2009). This degree of correspondence is probably fortuitous. Not only is there considerable scatter in cloud cover among the simulations, cloud cover can vary by a factor of two for any given model as a function of its resolution and numerical methods (Matheou et al., 2010).

Journal of Advances in Modeling Earth Systems james_000056.3d 24/5/11 09:57:52
The Charlesworth Group, Wakefield +44(0)1924 369598 - Rev 7.51n/W (Jan 20 2003)

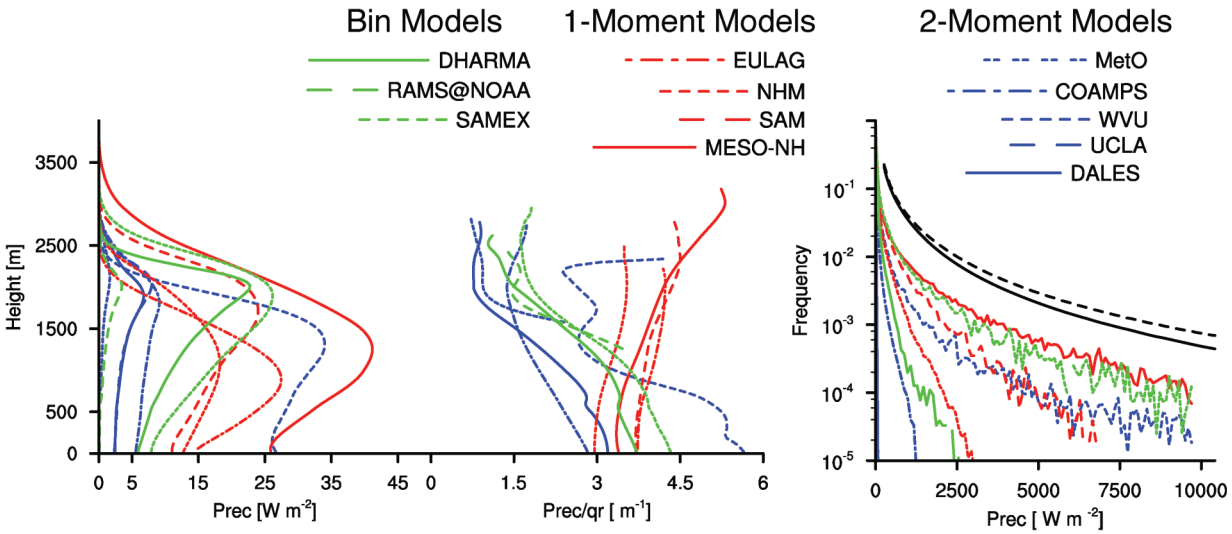

Figure 6. Precipitation flux profile (upper-left); 'bulk' fall velocity (upper-right); histograms of surface rain rates as a function of intensity (for last hour only, bottom right). In the rain-rate histograms the black lines denote the SPol data converted using either the TRMM (solid) or RICO (dashed) reflectivity vs rain-rate relationship. Lines are otherwise colored following the degrees of freedom available for the microphysical scheme, green for bin, blue for two moment and red for one moment schemes (note because of an output diagnostic problem the UCLA-LES is not included in the 'bulk' fall velocity plot).

Likewise, observational estimates vary significantly, both as a function of ones retrieval method and ones choice of sensor (Zhao and Di Girolamo, 2007). These caveats aside, the cloud cover is almost certainly between 0.1 and 0.3, and given this range of uncertainty it appears to be well represented by the simulations.

To compare the vertical profile of cloudiness with the lidar data we define an effective cumulative cloud cover, at some level using the algorithm of Neggers et al. (2011), which is derived from LES. However the grid-spacing dependent length scale used to composite layers was rescaled (by a factor of 0.6) in our application so that it matched the lidar for surface based cloud-cover. The rescaling was justified by the fact that their is some arbitrariness in how one sets the reflectivity threshold in the lidar, and hence the overall cloud cover (Nuijens et al., 2009). Moreover, our motivation for reconstructing the effective increment in cumulative cloud fraction, due to clouds at different layers, was not meant as a test of the reconstruction method, but rather the vertical distribution of clouds by the simulations.

The effective cloud cover versus height, as defined by the reconstruction, is presented in Fig. 7 alongside the cumulative cloud cover as measured by the lidar. The agreement is remarkable, suggesting that LES may adequately represent the distribution of cloud top heights. The level of agreement is even more surprising given that the observations composite over more variability, hence the tendency for a few clouds to reach much lower. At the very least, the result is encouraging for the use of LES to help inform parameterizations of the vertical distribution of cloud cover, and in interpreting satellite data (Medeiros et al., 2010).

Important aspects of the simulated microphysical structure of the clouds appear consistent with the observations. This conclusion is based on Fig. 8 which compares vertical profiles of flight data from six C-130 flights during the composite period (details of processing of the aircraft data is provided in an appendix), with the multi-model mean from the simulations. The simulations plausibly represent the profiles of cloud and rain water, and the raindrop population density profile. Although the cloud-drop population density profile is also reasonably well captured, this is largely by design; droplet/CCN population densities were specified so as to reasonably represent the active cloud droplet concentrations – which is by definition somewhat larger than the mean. Of the varied data, the profile of cloud water is perhaps the quantity that is best constrained by the measurements, and the best captured by the models. Both simulated and observed liquid-water lapse rates in the lower 500 m of the cloud layer are about half their adiabatic value. Higher in the cloud layer there is some evidence that the models realize more liquid water than is usually measured, but the sampling of clouds at these levels is poorer and so the comparison with the simulations is more uncertain.

Beyond the order of magnitude agreement emerge some apparent discrepancies, particularly in the distribution of the rain-water which is less constrained in its evolution than is the cloud water. The third panel of Fig. 8 suggests that the observed raindrop population density is constant below cloud base and increases gradually through the cloud layer, with little indication of the cloud base level in the data. This is less true in the simulations where cloud base is marked by a rather sharp change in the raindrop population density.

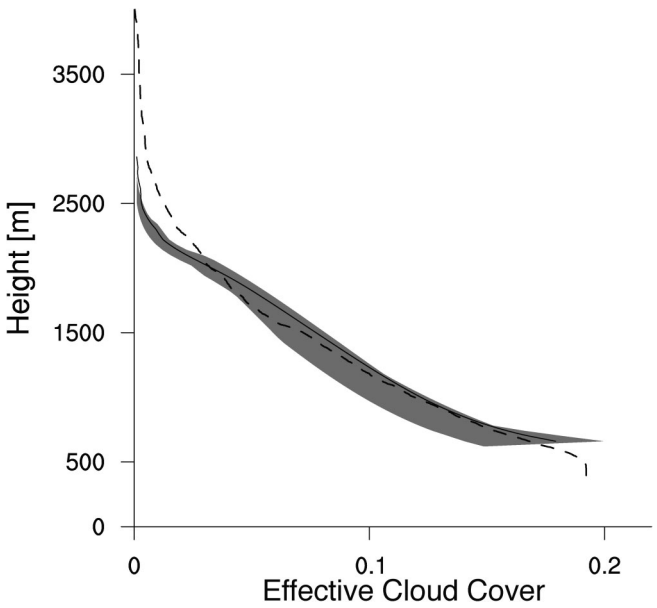

Figure 7. Lidar and effective LES cloud cover. The lidar cloud cover, shown by the dashed line, is the cumulative cloud cover and must monotonically increase as one traverses the layer (from top to bottom). The total cloud cover is given by the cloud fraction at cloud base. For LES the effective cloud cover is reconstructed from cloud fraction versus height data, and scaled to match the lidar near cloud base. The shaded area denotes the interquartile difference, as in Fig. 3.

The simulated rainwater content also appears to be at the upper end of what is observed, although the more or less constant vertical structure is quite similar to what one finds in the measurements. Taken together these results suggest that the simulations have more smaller drops that evaporate more readily in the sub-cloud layer, but contribute little to the rain water content.

The observed area of precipitation during RICO varied between 0 and 10 % with a mean between 2–3 %. This area was defined as the frequency of echoes (in the 0.5° surveillance scans) with a reflectivity greater than 7 dBZ. Simulated surface precipitation areas, defined as regions where the surface precipitation rate would correspond to a reflectivity greater than 7 dBZ (given the reflectivity and rain rate relationship used by Nuijens et al., 2009), vary between 0 and 3% with an average of 1.3%. Given the uncertainties in the data, the complications of the sampling, and the imprecision of our analysis, one should hesitate to conclude more than that the models plausibly represent the leading order structure of the precipitation field.

On average the shape of the rain rate distributions approaches those observed, particularly in the most strongly precipitating simulations. This is evident in the rain intensity histograms shown in Fig. 6. These histograms show however that most simulations produced less precipitation than was observed, and for those that precipitate most weakly, strong showers were under-represented.

A similar inference can be made on the basis of the bulk rain intensity. To judge this we normalize the net precipitation (for events stronger than the detection limit of the observations) by the area fraction of the echoes. Doing so for the S-band radar measurements during the undisturbed period of RICO yields a raining-area rain-rate,

$$R_p = \frac{\overline{R}}{a_p}$$

where $\overline{R}$ is the average rain rate, and a_p is the rain-rate area, of about 25 mm d^{-1} as compared to a simulated value of about 20 mm d^{-1}. That said, the intensity of the rain-rate varies greatly, as echoes greater than 50 dBZ (equivalently 160 mm d^{-1} given the Z-R relationship used by Nuijens et al., 2009) were observed from shallow systems, and 30 dBZ (82 mm d^{-1}, to convert to other units see Table 1) echoes were routine. Such values are in line with those evident in the rain-intensity histograms (Fig. 6) constructed using data from the simulations.

Looking across simulations, there is a tendency for the rain-area, a_p, to increase with the total rainfall, $\overline{R}$. This point is illustrated in Fig. 9, and corresponds to what was also found in the RICO radar data (cf., Fig. 5b of Nuijens et al., 2009), although the relationship that emerges from an analysis of the observations is somewhat flatter (as indicated by the lines in Fig. 9), consistent with the somewhat larger (2.5 versus 2.0 cm d^{-1}) raining-area rain-rates in the data.

Note that a one-to-one line on Fig. 9 implies that an increase in the rain rate can be explained entirely by an increase in the rain area. The observations fall along a line whose slope in Fig. 9 is somewhat less than one, while the simulations define a slope somewhat greater than one. This suggests that to the extent they disagree, as rain-rates increase the observations indicate that the additional rain

Journal of Advances in Modeling Earth Systems james_000056.3d 24/5/11 09:57:56
The Charlesworth Group, Wakefield +44(0)1924 369598 - Rev 7.51n/W (Jan 20 2003)

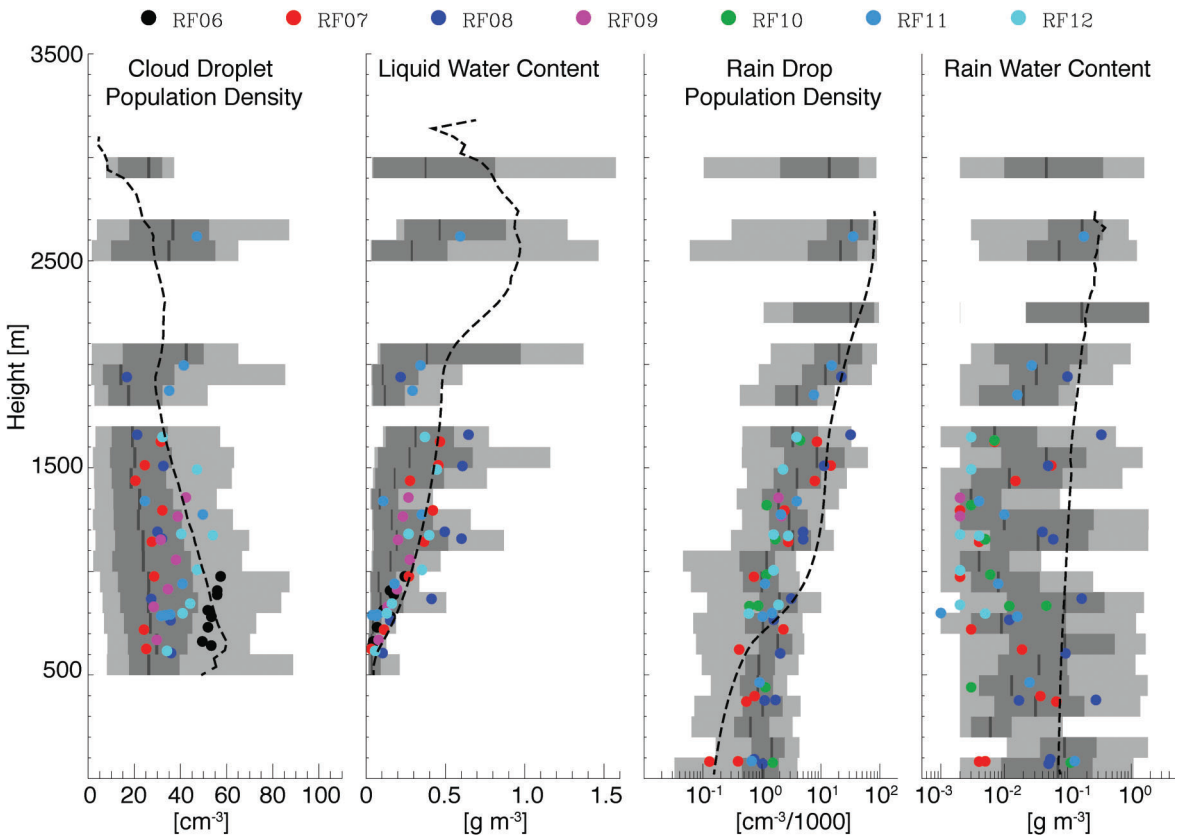

Figure 8. Vertical structure of cloud microphysical properties as derived from five flights (shading and dots) as well as the LES (dashed line). Shown are the cloud droplet population density (a); cloud water content (b); rain-water population density (c); rain-water content (d). The shaded gray regions denote the range of the observations. The light gray shading spans the 5 to 95 percentile of the aircraft data, the dark gray spans the 25–75 percentile. Median values are indicated by the gray vertical line.

is carried by somewhat stronger, not just more, showers, relative to the simulations.

There is some indication that the simulations produce rain whose spatial distribution is more uniform than what is observed. To arrive at this conclusion we compare the incidence of precipitation in the LES domain with that taken from subdomains of the radar. Because the large size of the radar domain allows us to sub-sample smaller subdomains, it is possible to explore the probability of precipitation as a function of spatial scale from the radar data.

The result of this analysis is presented in Fig. 10. It suggests that given the size of the LES domain, precipitation occurs too frequently in most of the simulations. Although a couple of simulations precipitate with a frequency commensurate with the observations, these greatly under-estimate the total precipitation. Our interpretation of this result is that the observed precipitation during RICO is organized on larger scales (by a factor of 2-8) than what can be captured by the LES domains used for our comparison. This inference is also supported by large-domain simulations (G. Matheou, personal communication) that show as larger-scales are allowed to develop, regions of precipitation and relatively clear areas organize themselves on these scales.

5. Sensitivity to microphysics

The amount of precipitation across the ensemble of simulations appears to be significantly influenced by one's choice of microphysical representation. To arrive at this conclusion, we compare the simulated liquid water path for a non-precipitating simulation of a given model with the precipitation that the same model produces when microphysical processes are allowed to become active. Although the experimental design should preclude differences in the liquid water path in the non-precipitating simulations, differences do arise because of numerical artifacts, or differences in the representation of subgrid-scale processes by the different models (*e.g.*, Matheou et al., 2010). Small changes in cloud macrostructure, or model dynamics, can have profound implications for the development of the cloud layer and the precipitation (Stevens and Seifert, 2008; Nuijens, 2010; Matheou et al., 2010). We use liquid water path in the non-precipitating simulations as a proxy for cloud macrostructure and hypothesize that microphysical controls on precipitation contribute to the departure from a linear relationship between our macrostructure proxy and the rain rate in the precipitating simulations. Fig. 11 indicates that cloud-macrophysical differences (here, the LWP's), that arise

Journal of Advances in Modeling Earth Systems james_000056.3d 24/5/11 09:57:57
The Charlesworth Group, Wakefield +44(0)1924 369598 - Rev 7.51n/W (Jan 20 2003)

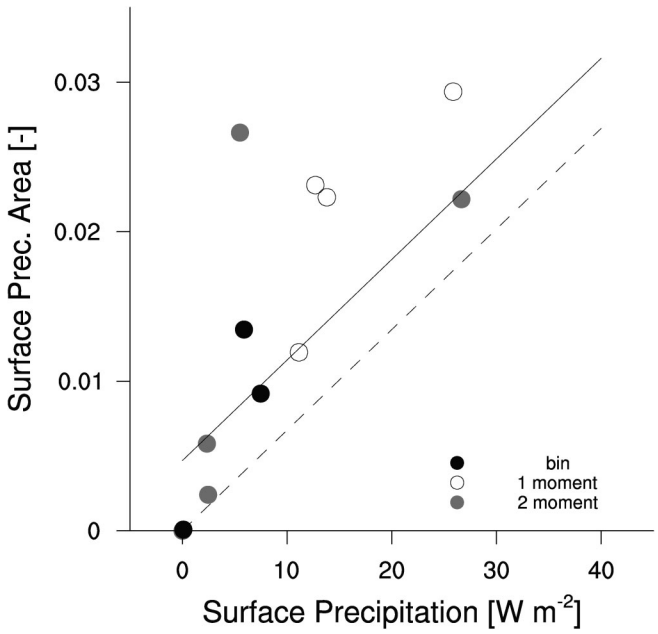

Figure 9. Raining area as a function of net surface rain-rate, with dots denoting the different models and the lines denoting the radar observations, with reflectivity to rain-rate being converted using either the TRMM (solid line) rain -rate reflectivity relationship. The dashed line has the same slope as the solid line but with no offset.

can partly explain differences in the precipitation produced by different models, increasingly so for those models with more sophisticated microphysical representations. However, and particularly for the one moment models, variations in rain-rate do not only scale with liquid water path. Such departures are also apparent, albeit less, among the two-moment and bin-microphysical models. We interpret this scatter as being the result of differences in the representation of cloud microphysical processes. Although we cannot rule out the idea that other aspects of cloud macrostructure may also play a role, our interpretation is supported by simulations with a single code wherein microphysical representations were modeled

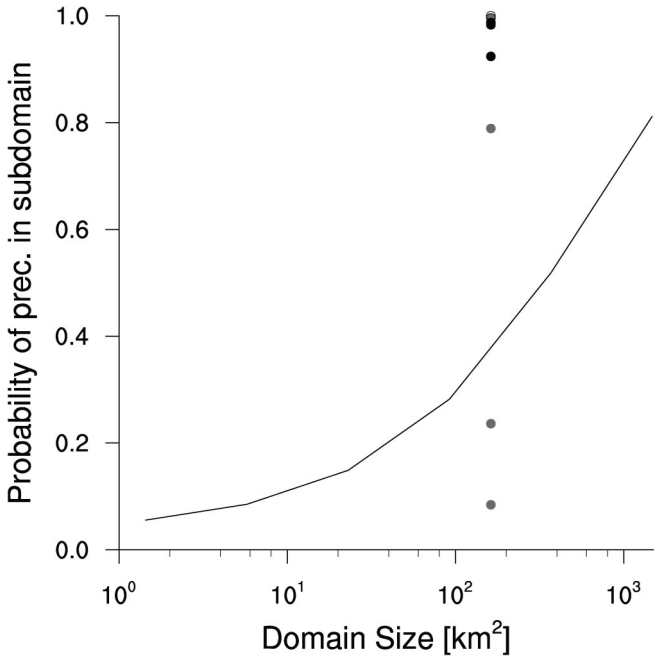

Figure 10. Probability of precipitation in subdomains of size ℓ. Circles show the LES data, with symbols as in Fig. 9. Almost all the points, except for three of the two-moment simulations, group under the black dots near a probability of unity, indicating that precipitation was almost always present in the LES.

Journal of Advances in Modeling Earth Systems james_000056.3d 24/5/11 09:57:59
The Charlesworth Group, Wakefield +44(0)1924 369598 - Rev 7.51n/W (Jan 20 2003)

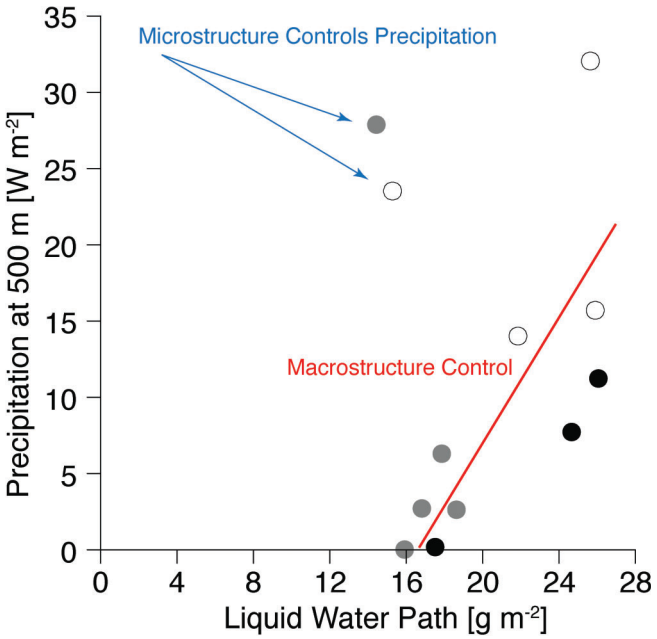

Figure 11. Relationship between LWP in non-precipitating simulations and precipitation that develops at cloud base in precipitating simulations. The red line qualitatively illustrates how we might expect the results to be distributed if the precipitation is controlled by differences in the cloud states produced by different models. The two points indicative of microphysical controls (identified by the blue arrows) are meant to be illustrative of results that are particularly far from such a trend.

differently, leading to large changes in the amount of rain produced (Stevens and Seifert, 2008).

6. Sensitivity of the cloud layer to precipitation development

The effect of allowing precipitation to develop in the simulations is, even at the modest amounts considered here, evident if not dramatic. These effects include a marked (100 m, *e.g.,* upper panel of Fig. 3) reduction in the growth of the cloud layer and a cooling of the sub-cloud layer, which in turn is responsible for a slight increase in sensible heat fluxes (*e.g.,* third panel of Fig. 3). The temperature profile in simulations that are allowed to precipitate is somewhat more stable (as measured by its departure from the moist-adiabat) than the non-precipitating simulations. The effect of precipitation on the depth of the cloud layer is also evident in Fig. 12, where the shallowing of the cloud layer as a function of precipitation is readily evident. This result supports the hypothesis in earlier work (Riehl et al., 1951; Betts, 1973; Stevens, 2007), that the principal mechanism through which the trade-wind layer deepens is through the evaporation of liquid water in the stable air within, and above, the trade inversion, thus gradually imbuing these layers with the properties of the cloud layer below.

The somewhat deeper clouds in the non-precipitating cases are also more vigorous, say as measured by the vertical velocity variance within the cloud and sub-cloud layers, or by vertical velocity conditioned over cloudy, or cloud-core areas (*e.g.,* upper panels of Fig. 5). Sharper gradients near cloud top enhance scalar variances there. There is also a hint that the somewhat more vigorous convection in the non-precipitating ensemble is associated with more mixing, when measured by the entrainment and detrainment rates in the lowest km of the cloud layer (*e.g.,* Fig. 5).

Systematic differences in the overall amount of cloud or liquid water between the precipitating and non-precipitating simulations are more difficult to establish; differences among models for the non-precipitating case are as large as those for a single model when precipitation is allowed to develop. Fig. 13 shows that for light precipitation most models tend to produce an increase in cloud cover, while for heavier precipitation more models experience a reduction in cloud cover. The signal is weak, but it is evident across the microphysical model hierarchy, and echoes the results of Stevens and Seifert (2008) where one model was used and the precipitation efficiency in that model was varied. Overall, it suggests that the response of cloud cover to an increase in precipitation is dependent on the nature of the perturbation. This considerably complicates efforts to parametrize and evaluate the so called lifetime effects in large-scale models (cf., Stevens Feingold, 2009).

7. Conclusions

A case study is defined to explore the evolution of clouds similar to those observed during an undisturbed period of measurements during the Rain in Cumulus Over the Ocean (RICO) field study. The initial data are drawn from the RICO measurements and the forcing is derived from a local downscaling of meteorological analyses. Twelve groups submitted a pair of large-eddy simulations that conformed to the specifications of the case study. This pair consisted of two twenty-four hour periods, one for which precipitation is inhibited in the model, another for which precipitation is allowed to developed. Precipitation development within a model depends on the microphysical parameterization employed, with approaches differing considerably among the participating LES's.

The simulations agree on the broad structure of the cloud field that develops given the initial data and forcing and this structure plausibly reproduces many features of the observed layer. Thermodynamically and energetically, the simulations are similar to past simulations of clouds in the trade-winds, although the cloud mass flux decreases less evidently with height as compared to simulations of shallower cloud layers, *e.g.,* as observed during BOMEX or ATEX. In contrast to past studies of clouds in the trade-winds, the RICO data allow us to more quantitatively evaluate the representation of the cloud and precipitation

Journal of Advances in Modeling Earth Systems james_000056.3d 24/5/11 09:58:01
The Charlesworth Group, Wakefield +44(0)1924 369598 - Rev 7.51n/W (Jan 20 2003)

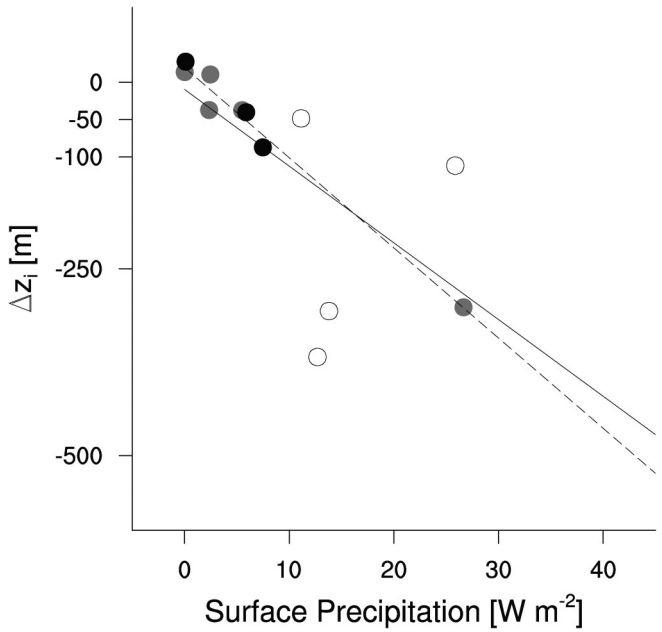

Figure 12. Difference in the final depth of the marine layer between the precipitating and non-precipitating simulation for each model as a function of the rate of precipitation in the precipitating simulation. Regression lines show best fit for all simulations (solid) and only the bin and two-moment schemes (dashed).

fields by the simulations — although sampling issues associated with the relative sparcity of clouds make this data challenging to use in a decisive way. That said, the vertical structure of cloudiness and cloud water, the order of magnitude of precipitation rate, and rain-water content are plausibly represented by the simulations, as are some aspects of the variability in the data, for instance the general tendency for more rain to scale with the raining area.

The simulations differ substantially in the amount of rain they produce, and in the microphysical details of the cloud evolution itself. Despite these differences, the simulations all produce precipitation profiles that maximize near cloud top,

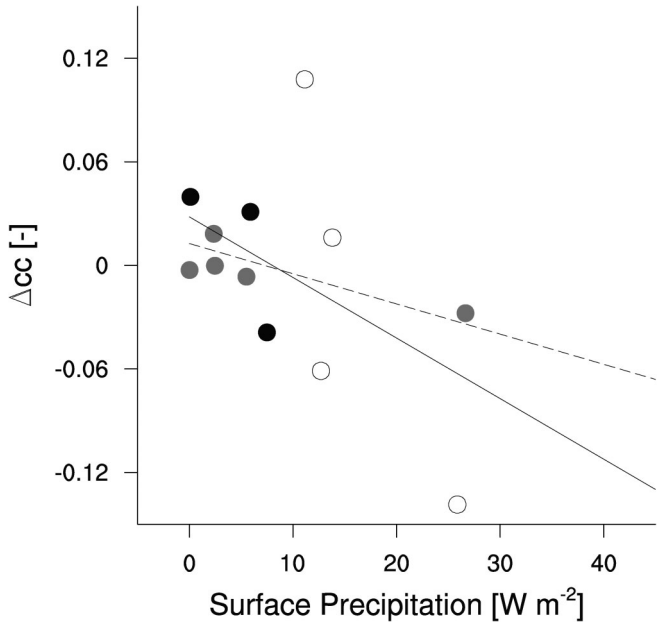

Figure 13. Difference in cloud cover between simulations with and without precipitation by each model as a function of the precipitation rate in the precipitating simulation. Regression lines show best fit for all simulations (solid) and only the bin and two-moment schemes (dashed).

Journal of Advances in Modeling Earth Systems james_000056.3d 24/5/11 09:58:02
The Charlesworth Group, Wakefield +44(0)1924 369598 - Rev 7.51n/W (Jan 20 2003)

with most of the re-evaporation of rain concentrated in the cloud layer itself. This differs from the typical picture of convective clouds, wherein the rain falls through the cloud-itself, thereby maximizing the precipitation flux near cloud base, and concentrating re-evaporation in the subcloud layer.

Differences in the simulated structure and amount of precipitation appear to be partly related to (controlled by) microphysical assumptions made in the models, increasingly so for the simpler microphysical models. However, significant variations in precipitation can also be attributed to small changes in cloud macrostructure, which arise due to numerical artifacts or differences in the representation of subgrid-scale processes. Among the simulations with the more comprehensive microphysical schemes there does seem to be an indication that differences in precipitation are better explained by cloud macrostructural differences. But as microphysical models become more parametric the differences in their formulation appear to increasingly contribute to differences in the amount and structure of precipitation. The general behavior of the two moment schemes is more in line with the bin models, suggesting that the former may be adequate for many purposes. The trade-off between simplicity and performance (reliability) that one achieves by only modeling one moment of the cloud-droplet distribution appears less favorable.

Across models some robust tendencies emerge in response to the development of precipitation. As precipitation develops there is a systematic tendency for the cloud layer to deepen less rapidly, the stability within the cloud layer is enhanced, and there is some sign that the cloud circulations become less vigorous. The response of cloud cover is more ambiguous. There is some evidence that it increases when precipitation is light, and decreases as precipitation becomes stronger, which suggests that cloud amount is in part controlled by the amount of precipitation. Many of these findings are consistent with those of earlier studies based on a single model.

Acknowledgments: We thank all of those who participated in RICO and helped collect and prepare the data that made this study possible, in particular Robert Rauber and Larry Di Girolamo are thanked for the discussions that helped frame the present study. The Goddard Institute for Space Studies is thanked for hosting an initial workshop to help organize the intercomparison. Computing resources for ASA were provided by the NASA High-End Computing Program through the NASA Advanced Supercomputing Division at Ames Research Center. MvZ would like to acknowledge the financial support of Grant 857.00.007 of the Netherlands Organisation for Scientific Research (NWO). Brian Medeiros and Chiara Antoniazzi are thanked for help in preparing some of the analysis of lidar data. Peter Bogenschutz, Christopher S. Bretherton, Wojciech Grabowski and Steve Krueger are thanked for their contributions to the discussion of the case study, Irina Sandu and Wojciech Grabowski are thanked for comments on a draft version of this manuscript. Three constructive and thoughtful reviews greatly improved the manuscript.

References

Abel, S. and B. Shipway, 2007: Acomparison of cloud resolving model simulations of trade wind cumulus with aircraft observations taken during rico. *Quart. J. Roy. Meteor. Soc.*, **133**, 781–794, doi: 10.1002/qj.55.

Ackerman, A. S., M. P. Kirkpatrick, D. E. Stevens, and O. B. Toon, 2004: The impact of humidity above stratiform clouds on indirect aerosol climate forcing. *Nature*, **432**, 1014–1017, doi: 10.1038/nature03174.

Ackerman, A. S., *et al.*, 2009: Large-eddy simulations of a drizzling, stratocumulus-topped marine boundary layer. *Monthly Weather Review*, **137**(3), 1083–1110, doi: 10.1175/2008MWR2582.1.

Albrecht, B. A., 1989: Aerosols, cloud microphysics and fractional cloudiness. *Science*, **245**, 1227–1230, doi: 10.1126/science.245.4923.1227.

Augstein, E., H. Riehl, F. Ostapoff, and V. Wagner, 1973: Mass and energy transports in an undisturbed Atlantic trade-wind flow. *Mon. Wea. Rev.*, **101**, 101–111, doi: 10.1175/1520-0493(1973)101<0101:MAETIA>2.3.CO;2.

Betts, A. K., 1973: Non-precipitating cumulus convection and its parameterization. *Quart. J. Roy. Meteor. Soc.*, **99**, 178–196, doi: 10.1002/qj.49709941915.

Bony, S. and J.-LDufresne, 2006: Marine boundary layer clouds at the heart of tropical cloud feedback uncertainties in climate models. *Geophy. Res. Let.*, **32**, L20 806.

Brenguier, J.-L., T. Bourrianne, A. Coelho, J. Isbert, R. Peytavi, D. Trevarin, and P. Wechsler, 1998: Improvements of the droplet size distribution measurements with the Fast FSSP (Forward Scattering Spectrometer Probe). *J. Atmos. Oceanic Technol.*, **15**, 1077–1090, doi: 10.1175/1520-0426(1998)015<1077:IODSDM>2.0.CO;2.

Bretherton, C., P. N. Blossey, and J. Uchida, 2006: Cloud droplet sedimentations, entrainment efficiency and subtropical stratocumulus albedo. *Geophy. Res. Let.*, **34**, L03 813, doi: 10.1029/2006GL027648.

Brown, A. R., *et al.*, 2002: Large-eddy simulation of the diurnal cycle of shallow cumulus convection over land. *Quart. J. Roy. Meteor. Soc.*, **128**, 1779–1798, doi: 10.1256/003590002320373210.

de Rooy, W. C. and A. P. Siebesma, 2008: A simple parameterization for detrainment in shallow cumulus. *Mon. Wea. Rev.*, **136**, 560–576, doi: 10.1175/2007MWR2201.1.

Deardorff, J. W., 1980: Cloud top entrainment instability. *J. Atmos. Sci.*, **37**, 131–147, doi: 10.1175/1520-0469(1980)037<0131:CTEI>2.0.CO;2.

Ghosal, S., 1996: An analysis of numerical errors in large-eddy simulations of turbulence. **125**, 187–206.

Heus, T., C. F. J. Pols, H. J. J. Jonker, H. E. A. Van den Akker, and D. H. Lenschow, 2009: Observational validation of the compensating mass flux through the shell

Journal of Advances in Modeling Earth Systems james_000056.3d 24/5/11 09:58:04
The Charlesworth Group, Wakefield +44(0)1924 369598 - Rev 7.51n/W (Jan 20 2003)

around cumulus clouds. *Quart. J. Roy. Meteor. Soc.*, **135**, 101–112, doi: 10.1002/qj.358.

Holland, J., 1972: Comparative evaluation of some BOMEX measurements of sea surface evaporation, energy flux and stress. *J. Phys. Oceanogr.*, **2**, 476–486, doi: 10.1175/1520-0485(1972)002<0476:CEOSBM>2.0.CO;2.

Khairoutdinov, M. and Y. L. Kogan, 2000: A new cloud physics parameterization in a large-eddy simulation model of marine stratocumulus. *Mon. Wea. Rev.*, **128**, 229–243, doi: 10.1175/1520-0493(2000)128<0229:ANCPPI>2.0.CO;2.

Lewellen, W., 1977: Use of invariant modeling. *Handbook of Turbulence*, W. Frost and T. Moulder, Eds., Plenum Press, New York, New York, 237–290.

Malkus, J. S., 1956: On the maintenance of the trade winds. *Tellus*, **8**, 335–350, doi: 10.1111/j.2153-3490.1956.tb01231.x.

Matheou, G., D. Chung, L. Nuijens, B. Stevens, and J. Teixeira, 2010: On the fidelity of large-eddy simulation of shallow precipitating cumulus convection. *Mon. Wea. Rev.*, submitted.

Medeiros, B., L. Nuijens, C. Antoniazzi, and B. Stevens, 2010: Low-latitude boundary layer clouds as seen by CALIPSO. *J. Geophys. Res.*, in press.

Medeiros, B., B. Stevens, I. Held, M. Zhao, D. Williamson, J. Olson, and C. S. Bretherton, 2008: Aquaplanets, climate sensitivity, and cloud feedbacks. *J. Climate*, **21**, 4974–4991, doi: 10.1175/2008JCLI1995.1.

Meijgaard, E., L. Ulft, W. J. van de Berg, F. C. Bosveld, B. J. J. M. van den Hurk, G. Lenderink, and A. P. Siebesma, 2008: The KNMI regional atmospheric climate model RACMO, version 2.1. Tech. rep., Royal Netherlands Meteorological Institute, De Bilt Netherlands. KNMI publication: TR-302, 24/12/2008, pp43.

Neggers, R. A. J., T. Heus, and A. P. Siebesma, 2011: Overlap statistics of cumuliform boundary-layer cloud fields in large-eddy simulations. *J. Geophys. Res.*, submitted.

Nitta, T. and S. Esbensen, 1974: Heat and moisture budget analyses using BOMEX data. *Mon. Wea. Rev.*, **102**, 17–28, doi: 10.1175/1520-0493(1974)102<0017:HAMBAU>2.0.CO;2.

Nuijens, L., 2010: Precipitating shallow cumulus convection. Ph.D. thesis, University California Los Angeles, Los Angeles, CA 90095, USA.

Nuijens, L., B. Stevens, and A. P. Siebesma, 2009: On the environment of shallow precipitating convection. *J. Atmos. Sci.*, **66**, 1962–1979, doi: 10.1175/2008JAS2841.1.

Pawlowska, H. and J.-L. Brenguier, 2000: Microphysical propoerties of stratocumulus clouds during ACE2. *Tellus*, **52B,** 867–886.

Pawlowska, H. and J.-L. Brenguier, 2003: An observational study of drizzle formation in stratocumulus clouds for general circulation model (GCM) parameterizations. *J. Geophys. Res.*, **108** (**D15**), 8630., doi: 10.1029/2002JD002679

Randall, D. A., *et al.*, 2003: Confronting models with data: The GEWEX cloud systems study. *Bull. Amer. Meteor. Soc.*, **84**, 455–469, doi: 10.1175/BAMS-84-4-455.

Rauber, R., *et al.*, 2007: Rain in (shallow) cumulus over the ocean–the RICO campaign. *Bull. Amer. Meteor. Soc.*, **88**, 1912–1928, doi: 10.1175/BAMS-88-12-1912.

Riehl, H., 1954: *Tropical Meteorology*. McGraw-Hill, New York, 392 pp pp.

Riehl, H., C. Yeh, J. S. Malkus, and N. E. LaSeur, 1951: The North-East Trade of the Pacific Ocean. *Quart. J. Roy. Meteor. Soc.*, **77**, 598–626, doi: 10.1002/qj.49707733405.

Schumacher, C. and R. Houze Jr, 2003: The TRMM precipitation radar's view of shallow, isolated rain. *J. Appl. Meteor.*, **42**, 1519–1524, doi: 10.1175/1520-0450(2003)042<1519:TTPRVO>2.0.CO;2.

Seifert, A. and K. D. Beheng, 2001: A double-moment parameterization for simulating autoconversion, accretion and self collection. *Atmos Res*, **59–60,** 265–281, doi: 10.1016/S0169-8095(01)00126-0.

Seifert, A. and K. D. Beheng, 2006: A two-moment cloud microphysics parameterization for mixed-phase clouds. Part I: Model description. *Meteorol. Atmos. Phys.*, **92**, 45–66, doi: 10.1007/s00703-005-0112-4.

Short, D. and K. Nakamura, 2000: TRMM radar observations of shallow precipitation over the tropical oceans. *J. Climate*, **13**, 4107–4124, doi: 10.1175/1520-0442(2000)013<4107:TROOSP>2.0.CO;2.

Siebesma, A. P. and J. W. M. Cuijpers, 1995: Evaluation of parametric assumptions for shallow cumulus convection. *J. Atmos. Sci.*, **52**, 650–666, doi: 10.1175/1520-0469(1995)052<0650:EOPAFS>2.0.CO;2.

Siebesma, A. P., *et al.*, 2003: A large-eddy simulation study of shallow cumulus convection. *J. Atmos. Sci.*, **60**, 1201–1219, doi: 10.1175/1520-0469(2003)60<1201:ALESIS>2.0.CO;2.

Snodgrass, E., L. Di Girolamo, and R. Rauber, 2009: Precipitation characteristics of trade wind clouds during RICO derived from radar, satellite, and aircraft measurements. *J. Appl. Meteorol.*, **48**, 464–483, doi: 10.1175/2008JAMC1946.1.

Sommeria, G., 1976: Three-dimensional simulation of turbulent processes in an undisturbed trade wind boundary layer. *J. Atmos. Sci.*, **33**, 216–241, doi: 10.1175/1520-0469(1976)033<0216:TDSOTP>2.0.CO;2.

Stevens, B., 2007: On the growth of layers of non-precipitating cumulus convection. *J. Atmos. Sci.*, **64**, 2916–2931, doi: 10.1175/JAS3983.1.

Stevens, B. and G. Feingold, 2009: Untangeling aerosol effects on clouds and precipitation in a buffered system. *Nature*, **461**, 607–613, doi: 10.1038/nature08281.

Stevens, B., C.-H. Moeng, and P. P. Sullivan, 2000: Entrainment and subgrid lengthscales in large-eddy simulations of atmospheric boundary layer flows. *IUTAM Symposium on Developments in Geophysical Turbulence*, R. Kerr and Y. Kimura, Eds., Kluwer, Dordrecht, 253–269.

Stevens, B. and A. Seifert, 2008: On the sensitivity of simulations of shallow cumulus convection to their microphysical representation. *J. Meteorol. Soc. Japan*, **86a,** 141–163, doi: 10.2151/jmsj.86A.143.

Stevens, B., *et al.*, 2001: Simulations of trade-wind cumuli under a strong inversion. *J. Atmos. Sci.*, 1870–1891, doi: 10.1175/1520-0469(2001)058<1870:SOTWCU>2.0.CO;2.

Stevens, B., *et al.*, 2005: Evaluation of large-eddy simulations via observations of nocturnal marine stratocumulus. *Mon. Wea. Rev.*, **133**, 1443–1462, doi: 10.1175/MWR2930.1.

Zhao, G. and L. Di Girolamo, 2007: Statistics on the macrophysical properties of trade-wind cumuli over the tropical western Atlantic. *J. Geophys. Res.*, **112 (D10204)**

Appendix

A. Details of data preparation

The rainwater data from the aircraft was taken by summing the liquid water concentrations from the 260X probe over the range from 85 μm and the 2DP data for drops larger than 300 μm in diameter. Raindrops in the LES are defined to be those drops with a diameter larger than 80 μm. The data is processed using a 10 Hz sampling rate. To be more commensurate with the sampling of the LES the data was also reprocessed with a sampling rate of 1 Hz, corresponding roughly to 100 m scales. These data showed some reduction in the cloud droplet concentration and liquid water profiles, especially on flights such as RF06 when the cumulus were small. However relative to the overall scatter the effect of the sampling frequency was relatively minor.

For the plots of N_r the WVU data was not included in the plot due to an apparent sampling error.

B. Output templates

Tables 4–6 provide the list of output variables of the RICO case and are as such a description of the available NetCDF files. The output files of the two master ensembles contain the mean, variance, minimum and maximum and inner and outer quartile values of the variables of Tables 4 and 5.

Table 4. Scalars provided as a time-series often a the sampling interval with which profile statistics were accumulated (0.5–5.0 min).

symbol	NetCDF var. name	Description	Units
	time	Time	[s]
z_i	zi	Mean height of grid cells with largest potential temperature gradient	[m]
z_{cb}	zcb	Height of bottom of lowermost cloudy grid cells	[m]
z_{ct}	zct	Height of top of highest cloudy grid cells	[m]
	zmaxcfrac	Height of bottom of grid level with highest mean cloud fraction	[m]
	M_zmaxcfrac	Cloud core mass-flux at zmaxfrac height	[kg m^{-2} s^{-1}]
LWP	LWP	Mean liquid water path	[g m^{-2}]
	LWP_var	Liquid water path variance	[g^2 m^{-4}]
RWP	RWP	Mean rain water path	[gm^{-2}]
cc	cc	Fraction of columns with number of cloudy grid cells >0	[-]
$\overline{w'\theta'}$	shf	Mean upward surface sensible heat flux	[K ms^{-1}]
$\overline{w'q'}$	lhf	Mean upward surface latent heat flux	[kg kg^{-1-1} m s^{-1}]
N_c	Nc	Mean cloud droplet concentration	[cm^{-3}]
N_r	Nr	Mean rain drop concentration	[cm^{-3}]
	tke	Vertically integrated TKE (sgs plus resolved), not density weighted	[m^3 s^{-2}]
	prec_srf	Mean (downward) precipitation flux at the surface	[kg kg^{-1} m s^{-1}]
	prec_500	Mean (downward) precipitation flux at 500 m	[kg kg^{-1} m s^{-1}]
	prec_980	Mean (downward) precipitation flux at 980 m	[kg kg^{-1} m s^{-1}]
	prec_1500	Mean (downward) precipitation flux at 1500 m	[kg kg^{-1} m s^{-1}]
	prec_1980	Mean (downward) precipitation flux at 1980 m	[kg kg^{-1} m s^{-1}]
	prec_2500	Mean (downward) precipitation flux at 2500 m	[kg kg^{-1} m s^{-1}]
	prec_srf_prc	Precipitation flux (downward) at the surface, averaged over precipitating surface grid cells only	kg kg^{-1} m s^{-1}
	prec_500_prc	Precipitation flux (downward)at 500 m, averaged over precipitating grid cells at 500 m only	[kg kg^{-1} m s^{-1}]
	prec_fracsrf	Fraction of surface grid cells with a surface precipitation flux of 3.65e-5 [kg kg^{-1} m s^{-1}] or higher	[-]

Table 5. Profile statistics, which are constructed by temporally and horizontally averaging the various fields.

symbol	NetCDF var. name	Description	Units
	time	Time	[s]
	zf	Altitude of layer mid-points	[m]
	llim	Value of the left limit of the bins in the histogram	[kg kg^{-1} ms^{-1}]
u	u	Zonal wind	[m s^{-1}]
v	v	Meridional wind	[m s^{-1}]
θ_l	thetal	Liquid water potential temperature	[K]
q_t	qt	Total water (vapor+liquid)	[g kg^{-1}]
q_l	ql	Condensed water	[g kg^{-1}]
q_r	qr	Rain water	[g kg^{-1}]
$\overline{u'u'}$	u_var	Resolved variance of zonal wind	[m^2 s^{-2}]
$\overline{v'v'}$	v_var	Resolved variance of meridional wind	[m^2 s^{-2}]
$\overline{w'w'}$	w_var	Resolved variance of vertical wind	[m^2 s^{-2}]
	w_skw	Resolved $\left(w'^3\right)/\left(w'^2\right)^{-1.5}$	[-]
$\overline{\theta_l'\theta_l'}$	thetal_var	Resolved variance of θ_l	[K^2]
$\overline{q_t'q_t'}$	qt_var	Resolved variance of q_t	[kg^2 kg^{-2}]
$\overline{w'\theta_l'}$	tot_wthl	Total θ_l flux, including subgrid-scale	[K m s^{-1}]
	sgs_wthl	Subgrid-scale θ_l flux	[K m s^{-1}]
$\overline{w'q_t'}$	tot_wqt	Total q_t flux, including subgrid-scale	[kg kg^{-1} m s^{-1}]
	sgs_wqt	Subgrid-scale q_t flux	[kg kg^{-1} m s^{-1}]
$\overline{w'\theta_v'}$	tot_wthv	Total θ_v flux	[K m s^{-1}]
$\overline{u'w'}$	tot_uw	Total (sgs plus resolved) zonal momentum flux	[m^2 s^{-2}]
$\overline{v'w'}$	tot_vw	Total (sgs plus resolved) meridional momentum flux	[m^2 s^{-2}]
	res_tke	Resolved TKE	[m^2 s^{-2}]
	sgs_tke	Subgrid TKE	[m^2 s^{-2}]
	res_buoy	Resolved buoyancy TKE production	[m^2 s^{-3}]
	res_shr	Resolved shear TKE production	[m^2 s^{-3}]
	res_transport	Resolved TKE transport (turbulent plus pressure)	[m^2 s^{-3}]
	res_diss	TKE dissipation (explicit plus numerical)	[m^2 s^{-3}]
cfrac	cfrac	Fraction of cloudy grid cells	[-]
	prec	Precipitation flux	[kg kg^{-1} m s^{-1}]
	prec_prc	Prec. flux averaged over prec. grid cells only	[kg kg^{-1} m s^{-1}]
	frac_prc	Fraction of prec. grid cells with a prec. flux of 3.65e-5 [kg kg^{-1} m s^{-1}] or higher	[-]
N_r	Nr	Mean rain drop population density	[cm^{-3}]
N_c	Nc	Mean cloud droplet population density	[cm^{-3}]

Table 6. Conditionally averaged profile statistics, which are constructed by temporally and horizontally averaging the various fields given some indicator (cloud, or core) function (Siebesma et al., 2003).

symbol	NetCDF var. name	Description	Units
w_{cld}	w_cld	average over all cloudy grid points of w	[m s^{-1}]
	thl_cld	average over all cloudy grid points of θ_l	[K]
	qt_cld	average over all cloudy grid points of q_t	[g kg^{-1}]
	ql_cld	average over all cloudy grid points of q_l	[g kg^{-1}]
	thv_cld	average over all cloudy grid points of θ_v	[K]
cofrac	cofrac	Fraction of cloud core grid points	[-]
w_{core}	w_core	average over all cloud core grid points of w	[m s^{-1}]
	thl_core	average over all cloud core grid points of θ_l	[K]
	qt_core	average over all cloud core grid points of q_t	[g kg^{-1}]
	ql_core	average over all cloud core grid points of q_l	[g kg^{-1}]
	thv_core	average over all cloud core grid points of θ_v	[K]
	histo_srf	Histogram of surface precipitation	

Journal of Advances in Modeling Earth Systems james_000056.3d 24/5/11 09:58:05
The Charlesworth Group, Wakefield +44(0)1924 369598 - Rev 7.51n/W (Jan 20 2003)